Effect of microstructural anisotropy and heat treatment on the corrosion behaviour of additively manufactured Ti-6Al-2Sn-4Zr-6Mo alloy

Journal of Alloys and Compounds 1008 (2024) 176746

Contents lists available at ScienceDirect

Journal of Alloys and Compounds

journal homepage: www.elsevier.com/locate/jalcom

Effect of microstructural anisotropy and heat treatment on the corrosion behaviour of additively manufactured Ti-6Al-2Sn-4Zr-6Mo alloy

Alessandra Martucci, Leonardo Iannucci *, Mariangela Lombardi, Sabrina Grassini

Department of Applied Science and Technology, Politecnico di Torino, Corso Duca degli Abruzzi 24, Turin 10129, Italy

ARTICLE INFO

Keywords:
Metal additive manufacturing
Ti6246
Duplex microstructure
Heat treatment
Microstructural anisotropy
PBF-LB

ABSTRACT

The electrochemical behaviour of Ti-6Al-2Sn-4Zr-6Mo alloy produced by Powder Bed Fusion – Laser Based/Metals has been investigated to identify the corrosion mechanism characteristic of the material processed by additive manufacturing technology. A microstructural characterisation of the material in as-built and heat-treated conditions was carried out to identify the different phases and assess the degree of anisotropy of the additive manufactured material. After that, the corrosion behaviour was studied by potentiodynamic polarisation and electrochemical impedance spectroscopy. Results showed that a homogeneous and compact oxide layer characterises the as-built material due to the presence of a finely dispersed α'' phase in the β grains. Conversely, in the heat-treated alloy, the corrosion attack proceeds preferentially on the large α phase domains, where the oxide layer is less protective. Despite the anisotropy in the microstructure of the as-built material, the electrochemical behaviour was revealed to be the same for the section parallel and perpendicular to the building direction, noting the less influential factor of grain orientation on corrosion mechanisms.

1. Introduction

Ti-6Al-2Sn-4Zr-6Mo alloy (Ti6246) is a commercial α-β (duplex) Ti alloy widely used in aerospace applications and oil and gas industries where excellent corrosion and wear resistance are required. In particular, Ti6246 alloy has replaced the workhorse duplex Ti-6Al-4V (Ti64) in gas turbine hot sections thanks to its superior creep resistance and the ability to maintain good mechanical properties at temperatures up to 150 °C or higher [1,2]. Contrary to other duplex alloys, Ti6246 alloy is slightly more β-stabilised, presenting a higher amount of phase β at room temperature in equilibrium conditions [3]. Its closeness to the near-β category makes the Ti6246 alloy favoured over other duplex alloys in applications requiring higher ductility [4]. Despite the widespread use of Ti6246, it is difficult to forge and has significant limitations in filling moulds and achieving the reliability required for aerospace applications [5]. Its low thermal conductivity, hardness, wear resistance and high chemical reactivity with cutting tools complicate conventional machining, leading to higher production costs due to rapid tool wear [6]. Consequently, near-net-shape additive manufacturing techniques are becoming increasingly attractive for the production of Ti6246 components.

Recent studies have demonstrated the feasibility of processing Ti6246 alloy with densification levels above 99.9 % using the additive technique Powder Bed Fusion - Laser Based/Metals (PBF-LB/M) [4,7]. The processing of this alloy by PBF-LB/M is particularly encouraged by the presence of an inert atmosphere throughout the additive process that minimises oxidation phenomena, ensuring the integrity of the Ti6246 alloy. In addition, the extremely high cooling rates (10^5 to 10^7 °C/s) and directional thermal gradients involved in the PBF-LB/M process result in a peculiar as-built Ti6246 microstructure with columnar β-grains oriented parallel to the build direction and elongated martensitic phase needles arranged at about 45° to the build direction [8]. In contrast to the hexagonal martensitic α′ structure found in Ti64, Ti6246 processed for PBF-LB/M revealed an orthorhombic martensitic α″ structure, which should lead to an increased ductility and a slight softening [9]. The processing of Ti6246 by PBF-LB/M is relatively recent, and its properties are still poorly investigated. Published research has focused on the microstructural effects of rapid solidification and heat treatment optimisation for α″-to- α + β transformation. In particular, Carrozza et al. studied various PBF-LB/M parameters, finding that higher VED values result in finer α" needles and higher hardness [4]. However, the inherent softening effect of the as-built α″ phase necessitated the development of novel heat treatments aimed at decomposing the martensitic phase, making Ti6246 suitable for applications requiring high strength and

* Corresponding author.
E-mail address: leonardo.iannucci@polito.it (L. Iannucci).

https://doi.org/10.1016/j.jallcom.2024.176746
Received 3 July 2024; Received in revised form 9 September 2024; Accepted 26 September 2024
Available online 1 October 2024

hardness. Peng et al. discovered that an ultra-high hardness peak (563 HV) could be achieved with a 5-minute heat treatment at 650 °C, resulting in a unique martensite-decomposed α+β microstructure [10]. Carrozza et al. identified 875 °C as the optimal annealing temperature to reach the right balance between strength, ductility and hardness, achieving a bi-lamellar structure that reduces sliding length due to secondary α-laths [11]. While the effect of microstructural features of PBFed Ti6246 in the as-built and heat-treated state on the tensile properties and hardness have been deeply investigated, the chemical-physical properties related to the applications in which Ti6246 is usually employed have been only partially explored.

The high service temperatures involved in the aerospace applications and harsh service environments of the oil and gas industry require excellent corrosion and wear resistance. In their latest work, Kan et al. shed light on friction response and wear behaviour of as-built and heat-treated Ti6246 processed by PBF-LB/M and conventional processes [8]. This work revealed how the extremely fine microstructure derived from the additive process could increase the O diffusion, generating numerous oxide flakes that led to a friction reduction [8]. However, to the best of the Authors' knowledge, no studies conducted to date have investigated the effects of the PBF-LB/M process on the corrosion behaviour of Ti6246. However, the good corrosion resistance of Ti6246, resulting from the consistent, continuous, spontaneous oxide layer that forms on the surface upon exposure to the atmosphere, has already been demonstrated for components produced by conventional processes. In particular, the approximately 6 wt% molybdenum content in the chemical composition proved to impart excellent corrosion resistance of conventionally produced Ti6246 components in reducing environments such as hydrogen sulphide (H_2S) and in hostile environments such as seawater [12]. Considering the specific application of high-pressure compressor disks for gas turbines, the effect of the duplex microstructure on the stress corrosion cracking mechanism was also investigated [13,14]. Despite the insightful studies conducted on conventionally processed Ti6246, the PBF-LB/M additive process leads to microstructural peculiarities that can modify the alloy corrosive behaviour. In particular, Dai et al. demonstrated on the Ti64 duplex alloy that an anisotropy exists in corrosion resistance related to the microstructural anisotropy caused by the PBF-LB/M process that could be more or less pronounced depending on the electrolyte solution used [15]. In addition, the metastable phases formed due to the rapid solidification involved in the PBF-LB/M process lead to microstructural responses to heat treatment that could be markedly different from those obtained by conventional processes. In published studies conducted on other Ti-based alloys, it has been observed that PBF-LB/M microstructural peculiarities pre- and post-heat treatment lead to marked differences in thermo-chemical-physical properties. Based on this, it is reasonable to expect that the peculiar microstructure of heat-treated PBFed Ti6246 samples may also impact their corrosion behaviour.

In order to fill the literature gap, the present work aimed to investigate the effect of anisotropic microstructure in as-built and heat-treated conditions on the corrosive behaviour of Ti6246 alloy processed by PBF-LB/M. To state the anisotropy condition in PBFed Ti6246 samples, the grain size and orientation in as-built and heat-treated conditions were investigated using Field Emission Scanning Electron Microscopy (FESEM) and the Electron BackScattered Diffraction (EBSD). Subsequently, the effect of grain orientation on corrosion resistance on PBFed Ti6246 was explored in two electrolyte solutions of different aggressiveness: aqueous solution with 0.9 wt% NaCl and aqueous solution with 0.9 wt% NaCl and 0.6 wt% NaF. Corrosion kinetics and mechanism were then assessed using potentiodynamic polarisation and electrochemical impedance spectroscopy (EIS). After that, the morphology of the corrosion attack was observed by electron microscopy in order to provide a comprehensive description of the corrosion behaviour of the alloy and the effect of microstructural anisotropy and heat treatment.

2. Materials and methods

2.1. Sample preparation

A commercial gas-atomised Ti-6Al-2Sn4Zr-6Mo powder, provided by TLS Technik GmbH, was used as feedstock material for the PBF-LB/M production. The declared chemical composition of the powder is reported in Table 1.

The samples were produced by PBF-LB/M with the EOS M270 Dual Mode machine under a high-purity Argon atmosphere. The latter is characterised by a build volume of 250 x 250 x 215 mm^3 and equipped with a Yb-fibre laser with a spot size of 100 μm and a maximum power of 200 W. The PBF-LB/M process parameters were selected according to a previous study by the Authors [4] and are summarised in Table 2.

In order to carry out a complete characterisation of the corrosion behaviour of the Ti6246 alloy, 15 x 15 x 15 mm^3 cubic samples were produced. After processing the desired samples, an electrical discharge machine removed all specimens from the platform. To evaluate the effect of heat treatment on the corrosion behaviour of the Ti6246 alloy, it was decided to treat some of the samples at 750 °C for 2 h according to the literature [11]. The heat treatment was conducted in a Pro. Ba. AVF800/S high vacuum furnace by performing a preliminary heating ramp of 3 h from room temperature to 50 °C to ensure a vacuum level of approximately $10^{-5}/10^{-6}$ mbar was reached and then using a heating rate of 5 °C/min to reach the desired temperature of 750 °C. The heat treatment considered was isothermal holding followed by furnace cooling, achieving a slow cooling of approximately 1.5–2 °C/min.

To study the effect of grain size and orientation in as-built and heat-treated conditions, all the samples were cut, as illustrated in Fig. 1, obtaining from the same cubic sample both the surface parallel to the build direction (XZ plane) and the one perpendicular to it (XY plane).

Then, all the cut samples were polished using Struers' standard metallographic procedure until their cross-sections were mirror-finished [16].

2.2. Scanning electron microscopy

Electron microscopy characterisations were performed using the FESEM Zeiss Supra 40. Images were acquired using an accelerating voltage of 5 kV and an aperture of 30 μm. To highlight the microstructural features, the samples were etched using a Kroll solution (2 mL HF, 5 mL HNO_3, 100 mL deionised water, according to ASTM Standard E 407).

2.3. X-ray diffraction

X-ray diffraction (XRD) measurements were carried out on XZ cross-sectioned samples using the Panalytical X'pert PRO diffractometer, equipped with a copper anode. The diffraction patterns were acquired at 40 kV and 40 mA in a Bragg Brentano configuration. A step size of 0.013° and a 2θ range between 20° and 60° were considered for the analyses.

2.4. EBSD characterisations

The FIB Scanning Electron Microscope (Tescan S9000G) equipped with a symmetry EBSD detector and Aztec analysis software was used to study the pre- and post-heat treatment grain size and orientation conditions to determine a possible correlation with the corrosion behaviour

Table 1
Ti6246 chemical composition declared by powder supplier.

	Ti	*Al*	*Sn*	*Zr*	*Mo*
Composition range (wt %)	balance	5.5 – 6.5	1.75 – 2.25	3.5 – 4.5	5.5 – 6.5

Table 2
PBF-LB/M process parameters.

Power (W)	Scanning speed (mm/s)	Hatch distance (μm)	Layer thickness (μm)	Scanning strategy	Platform temperature (°C)
190	1100	100	30	Standard 67° EOS strategy	100

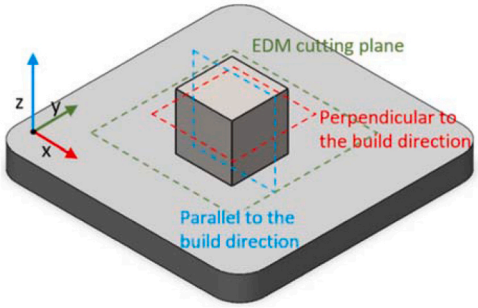

Fig. 1. Cutting directions used for sample preparation.

of the Ti6246 samples in as-built and heat-treated states. EBSD orientation maps were recorded at 300X magnification and a step size of 0.9256. The SEM was operated at 20 kV and 10 nA, and the samples were used in a pre-tilted sample holder at 70° tilt. The working distance for EBSD was kept at about 8 mm.

2.5. Electrochemical techniques

Electrochemical tests were performed at room temperature in naturally aerated electrolytes in a 3-electrode cell (250 mL of volume) composed of the sample (working electrode, WE), an Ag/AgCl electrode (reference electrode, RE), and a platinum wire (counter electrode, CE). Measurements were carried out using the 'IVIUM-n-Stat' electrochemical interface. Two different solutions were used: 0.9 wt% NaCl (sodium chloride, reagent grade purchased from Sigma) and 0.9 wt% NaCl with the addition of 0.6 wt% NaF (sodium fluoride, purchased from Sigma). All solutions were prepared in distilled water, and the pH was adjusted to 5 by adding HCl before the beginning of the tests. In this paper, the first electrolyte solution (containing only chloride ions) will be named 'S1', while the second one (containing both chloride and fluoride ions) will be named 'S2'.

Samples for electrochemical tests were soldered to a sheathed copper wire to ensure the electrical connection, then embedded in epoxy resin to expose either the surface parallel or perpendicular to the printing direction, and finally polished up to 4000 grits using SiC papers.

Before each electrochemical measurement, the Open Circuit Potential (OCP) was monitored for 1 hour.

EIS measurements were performed in the frequency range from 10^{-2} Hz to 10^{4} Hz, acquiring 10 points per frequency decade. The employed stimulus was a 10-mV sinusoidal signal applied around the OCP. Impedance spectra were then modelled using Equivalent Electrical Circuits (EECs). The capacitance was modelled in these circuits as a Constant Phase Element (CPE). Its impedance is defined as follows [14]:

$$Z_{CPE} = \frac{1}{(j\omega)^{n} \cdot Q}$$

where Q is the CPE parameter having dimensions of a capacitance, $j = \sqrt{-1}$, $\omega = 2\pi f$ (f is the frequency) and n is a parameter that ranges between 0 and 1. For a normal time-constant distribution through a surface layer (like in the case of a superficial oxide), the effective capacitance can be computed using the following formula [17,18]:

$$C_{eff} = Q^{\frac{1}{n}} (R_{ox})^{\frac{1-n}{n}}$$

where Q and n are the CPE parameters and R_{ox} is the parallel resistance. After that, the oxide thickness can be estimated [19,20]:

$$d_{ox} = \frac{\varepsilon \cdot \varepsilon_0}{C_{eff}}$$

where d_{ox} is the oxide thickness, ε is the oxide dielectric constant and ε_0 is the permittivity of vacuum.

Potentiodynamic Polarization measurements were acquired, sweeping the sample potential from −0.2 mV vs OCP to +1 V vs OCP at the scan rate of 10 mV/min. E_{corr} and I_{corr} values were computed using Tafel extrapolation. All electrochemical measurements were performed in triplicate, using more than one cubic sample for each condition. In this way, both the intra-sample and inter-sample variability were accounted for in the computation of the measurement error.

3. Results and discussions

3.1. Microstructure characterisation and phase identification

The FESEM analysis performed on Ti6246 as-built samples reveals the characteristic as-built microstructure of titanium alloys processed through PBF-LB/M, displaying visible melt pools and prior-β grains aligned in a columnar morphology parallel to the building direction (Fig. 2 a1-a2). This pattern is already known from previous studies of duplex Ti alloys and it is attributed to the high cooling rates and directional thermal gradients involved in the PBF-LB/M process, leading to epitaxial β-grain growth during solidification [4]. The elongated needles orientated with an around 45° angle are indicative of orthorhombic α″ martensite formation. The presence of the latter differentiates Ti6246 alloy from the α-stabilized duplex alloys such as the better-known Ti64, which instead presents the hexagonal α' martensitic phase. The occurrence of α″ significantly affects the mechanical properties of the alloy, providing an exceptional increase in ductility but also a detrimental reduction in hardness. To avoid the side effects of the α″ presence, a sub-β annealing treatment has been developed in the literature that aims to reduce internal stresses and decompose α" into α + β [11,21]. This transformation is diffusion-driven and requires high temperatures and long times. The micrographs in Fig. 2 b1-b2 related to the heat-treated specimens demonstrate the effectiveness of the treatment in transforming the martensitic microstructure typical of the as-built state into a fully duplex α + β microstructure. The columnar orientation is no longer visible after heat treatment, and the α lamellae show a high level of disorder, evidenced by the multiple orientations, as displayed in the low-magnification micrograph (Fig. 2 b1).

XRD measurements allowed for a more in-depth analysis of the observed phases. The XRD patterns related to as-built and heat-treated conditions, depicted in Fig. 3, confirm the previously stated hypothesis concerning the microstructural transformation during the heat treatment.

Observing the pattern related to the as-built state, the peaks could be exclusively correlated to the α″ martensitic phase. While looking closer at the XRD pattern acquired on the heat-treated sample, it is possible to discern the presence of both the α and β phases peaks, strongly confirming the decomposition of the α″ martensitic phase already observed with FESEM analysis.

To assess the anisotropy condition caused by the PBF-LB/M process and the effect of heat treatment on the grain size and orientation, the EBSD maps were acquired on XZ planes of Ti6246 samples pre- and post-heat treatment. The results obtained are reported in Fig. 4.

As evidenced by the EBSD maps shown in Fig. 4a, typical microstructural features of PBFed duplex titanium alloys were detected in the as-built Ti6246. The basket-weave structure within the columnar

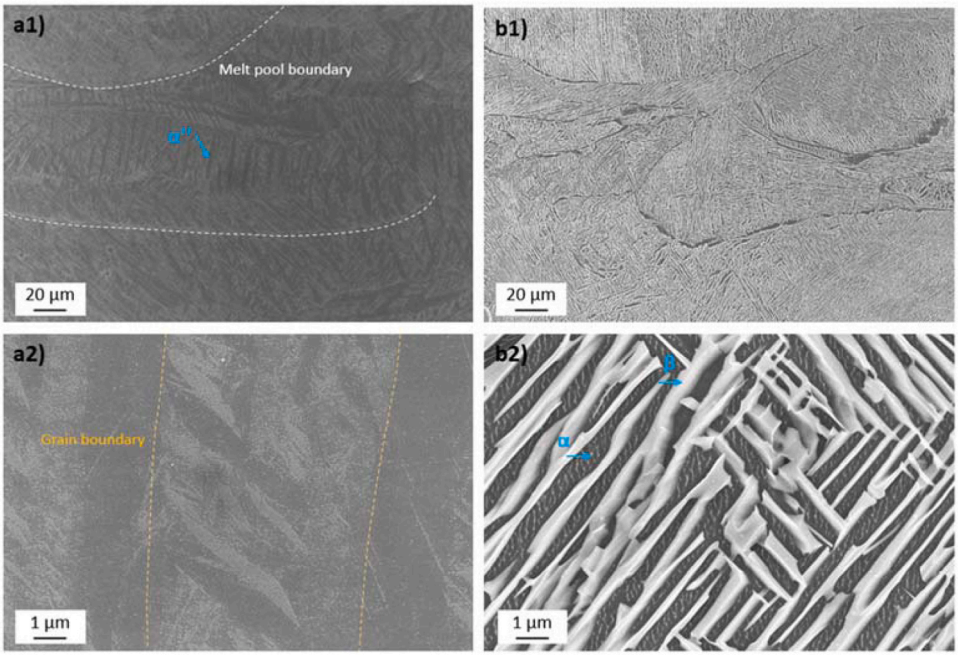

Fig. 2. FESEM micrographs of Ti6246 XZ samples in as-built (a) and heat-treated (b) conditions at low (1) and high (2) magnifications.

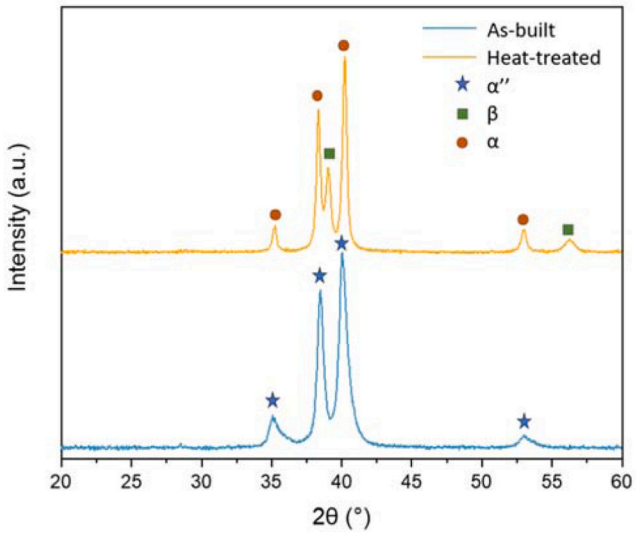

Fig. 3. XRD spectra of the Ti6246 XZ samples in as-built and heat-treated conditions.

β-grains is related to the needle-form α″ martensitic phase, already observed with FESEM analysis. In addition, columnar β-grains (highlighted in white in Fig. 4a) can be identified straddling the melt pools with an orientation parallel to the building direction. This marked grain directionality is distinctive of the microstructural anisotropy characterising the samples processed by PBF-LB/M. Observing the EBSD map conducted on the heat-treated sample (Fig. 4b), the basket-like structure almost completely disappears, confirming the successful transformation of the martensitic α'' phase into α + β proven by XRD spectrum analysis. However, the anisotropy observed in the as-built sample seems to have not been completely overcome. Indeed, it is important to consider that the heat treatment was conducted at 750 °C, well below the Ti6246 β transus temperature, which was determined metallographically at around 960 °C [22]. Despite this, grain growth and the onset of recrystallisation can be observed, which leads to the microstructural anisotropy being less evident after heat treatment. Microstructural anisotropy in titanium alloys resulting from additive processing significantly influences both mechanical and corrosion properties. In terms of mechanical properties, the anisotropic microstructure already contributed to directional variations in strength, affecting tensile and fatigue performance in different orientations. However, also the material susceptibility to corrosion could be affected by the anisotropic microstructure. In fact, the galvanic effects induced by anisotropy may lead to localised corrosion phenomena.

3.2. *Electrochemical characterisation of the as-built alloy*

The electrochemical properties of the material were characterised before and after heat treatment in two different solutions, having increasing aggressiveness. At pH=5, in electrolyte S1, the material is expected to be in 'passive conditions', while in electrolyte S2, it is expected to be in 'non-passive conditions' [23–25]. Thus, this specific pH value was chosen in order to have a change in the behaviour related only to the addition of fluoride ions. The in-depth study of the effect of pH on the electrochemical behaviour of material is beyond the scope of the present work, but some data related to the 'active', 'non-passive', and 'passive' behaviour are provided in Figure SM1 (Supplementary materials). Indeed, the data shown in Figure SM1 confirm the results provided in previous literature [24]. Moreover, the choice of the two electrolytes (S1 and S2) was not intended to mimic a specific environment, but rather to have sufficiently aggressive conditions in order to unveil the corrosion mechanism of the alloy. Indeed, fluoride ions are one of the few chemical species able to attack the titanium passivity in aqueous solutions, thus allowing to understand the role of the different phases in the material degradation.

Fig. 5a reports the potentiodynamic polarisation curves for samples immersed in S1 and S2 solutions. In both cases, the material exhibits an active behaviour close to the E_{corr} and then, increasing the anodic overpotential, it enters the passivity region. Samples immersed in the S1 solution have an E_{corr} value of −250 mV vs Ag/AgCl and I_{corr} of $1.5 \cdot 10^{-8}$ A/cm^2 (data referred to the XZ section; see Table 3 for the complete dataset). The increase of the anodic overpotential promotes the oxidation reactions on the sample surface, which lead to the rise of the oxide thickness [25]. The stable current values in the passive region

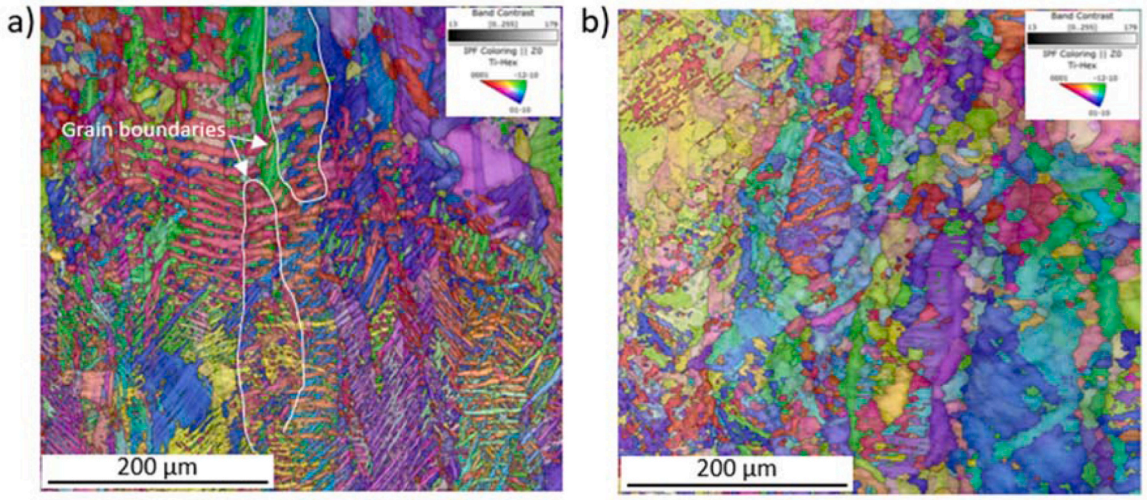

Fig. 4. EBSD maps on Ti6246 samples in as-built (a) and heat-treated (b) conditions.

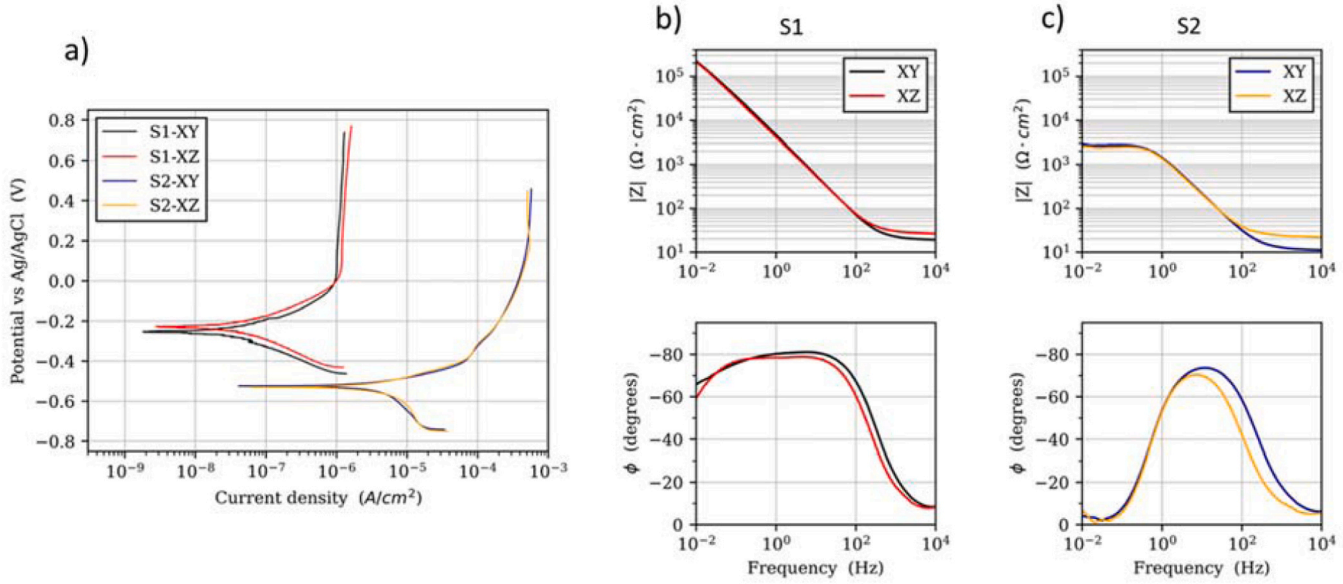

Fig. 5. Electrochemical measurements acquired on as-built samples: a) potentiodynamic polarization curves; b) and c) EIS measurements performed in solution S1 and S2 respectively. Measurements were acquired on surface parallel to the printing direction (XZ) and perpendicular to it (XY).

Table 3
E_{corr} and I_{corr} values computed for as-built samples in solutions S1 and S2.

	S1 Solution		*S2 Solution*	
	XZ section	XY section	XZ section	XY section
E_{corr} *[mV vs Ag/AgCl]*	−250 ± 40	−220 ± 20	−540 ± 40	−530 ± 20
I_{corr} *[A/cm²]*	(1.5 ± 1.1) 10^{-8}	(3.0 ± 2.5) 10^{-8}	(1.7 ± 0.6) 10^{-6}	(1.6 ± 0.8) 10^{-6}

demonstrate the formation of a continuous and uniform superficial oxide layer. No relevant differences were observed between the XZ and XY sections (see Table 3 for the data referring to all sample sets). The relatively large standard deviation computed for some of the I_{corr} values should be ascribed to the fact that, as the measurement repetitions were acquired on samples obtained from different cubic specimens, the measurement error accounts for both the intra-sample and inter-sample variability. Moreover, in some cases, the graphical method used to extrapolate the I_{corr} from the potentiodynamic polarization plot may decrease the accuracy of the computed value.

When immersed in solution S2, which contains both chlorides and fluorides ions, the as-built material exhibits a decrease in the E_{corr} value, which reaches −540 mV vs Ag/AgCl, and an increase in the I_{corr} value, that reaches $1.7{\cdot}10^{-8}$ A/cm^2 (data referred to XZ section, see Table 3 for the complete dataset). The aggressiveness of the fluoride ions towards the titanium alloy is further highlighted by the behaviour of the alloy in the anodic branch of the curve. Actually, a passive behaviour is observed, but it is reached at higher overpotential respect to the samples immersed in S1 solution; moreover, the passivation current is higher (about $5.2{\cdot}10^{-4}$ A/cm^2 instead of $1.2{\cdot}10^{-6}$ A/cm^2). In this electrolyte, the naturally-formed superficial oxide layer has a lower stability, as can be seen from comparing the EIS spectra acquired in the two solutions reported in Fig. 5b-c. In the S1 solution, the oxide layer is compact and continuous, and it exhibits a capacitive-like behaviour, with phase values close to −80° at its maximum. At lower frequencies, the impedance phase values slightly decrease, reaching values in the range

between −60° and −70°, and the impedance magnitude reaches values above 10^5 Ohm·cm^2, demonstrating a stable and protective behaviour. When immersed in the S2 solution, the oxide layer is less protective for the bulk material; actually, the maximum in the phase reaches lower values (close to −70°) and the behaviour becomes resistive at low frequencies (phase values close to 0°). The impedance magnitude at low frequencies is about $2{\cdot}10^3$ Ohm·cm^2, i.e. two orders of magnitude lower than in the other solution. No difference was detected between the XY and XZ sections from the EIS measurements. The stability of the acquired data as the sample section varies does not reveal a contribution of the grain orientation to the corrosion behaviour of the alloy. It is important to emphasise that the presence of the basket-weave structure due to the martensitic α'' phase in the as-built condition results in an extremely fine microstructure within the grain in both XZ and XY sections. It is, therefore, reasonable to suppose that, in this specific alloy, the most significant influence on the electrochemical behaviour is given by the phases present and not by the grain orientation itself.

3.3. Electrochemical characterisation of the heat-treated alloy

As revealed by the FESEM image analysis (Fig. 2), XRD phase identification (Fig. 3) and EBSD maps (Fig. 4), the annealing heat treatment significantly changes the microstructure of the alloy, leading to the decomposition of the martensitic phase into an α + β system. This transformation, which improves the material mechanical properties, could also influence the degradation mechanisms that characterise the Ti6246 alloy.

From the potentiodynamic polarisation measurements (see Fig. 6a), it is possible to notice that in the S1 solution, the behaviour remains the same, exhibiting an active-passive behaviour in the same potential and current ranges found for the as-built material. E_{corr} and I_{corr} remain stable after heat treatment, as seen from the data reported in Table 4. Looking at the data for solution S2, also in this case E_{corr} and I_{corr} do not change significantly (in both cases, only a slight decrease is observed). Analysing more in-depth the trend of the anodic branch of the potentiodynamic curve, it is possible to see that the transition from active to passive behaviour does not occur smoothly as it was in the as-built samples but through multiple passivation and re-activation phenomena. These are detectable as minor steps in the anodic branch of the curve before the stabilisation of the current value when the passive region is reached. In this potential interval, the simultaneous competition between the formation and dissolution of the anodically grown oxide layer is observed. It is important to underline that this phenomenon was observed in all tested samples, and it occurred in the same potential range, i.e. from −390 mV vs Ag/AgCl to +70 mV vs Ag/AgCl. Specifically, this behaviour is attributed to the presence of large α phase domains inside the network of β phase. Actually, as the former is less noble than the latter [26–28], it dissolves preferentially, and in the first stages, it does not contribute to forming a homogeneous and protective oxide layer.

Table 4
E_{corr} and I_{corr} values computed for heat-treated samples in S1 and S2 solutions.

	Solution S1		*Solution S2*	
	XZ section	XY section	XZ section	XY section
E_{corr} *[mV vs Ag/AgCl]*	−240 ± 40	−220 ± 20	−500 ± 20	−490 ± 50
I_{corr} *[A/cm^2]*	(2.9 ± 1.3) 10^{-8}	(1.6 ± 0.3) 10^{-8}	(1.4 ± 0.5) 10^{-6}	(1.1 ± 0.5) 10^{-6}

The presence of an inhomogeneous superficial oxide layer was observed also by EIS measurements (Fig. 6b-c). Actually, while the spectra acquired in the S1 solution are substantially equivalent to those acquired on as-built samples (both looking at the impedance magnitude and phase values), a different behaviour was detected in solution S2. The presence of the less-noble α phase leads to a preferential attack in these microstructure regions and thus to the appearance of a second time constant in the low-frequency range of the spectrum. This is identified graphically by analysing the phase values, which do not reach 0° in this part of the plot but stay close to 10°. This second time constant was detected both in the measurements acquired after one hour of immersion in the S2 solution and in an additional set of samples tested after 10 minutes of immersion in the electrolyte. Thus, the presence of an inhomogeneous oxide layer, due to the α + β microstructure, causes a preferential attack which occurs immediately after immersion of the alloy in the electrolyte (S2 solution). Further discussion about the corrosion mechanism of the material is provided in the next section.

Also for the heat-treated material, in both electrolyte solutions, no significant differences in electrochemical behaviour were revealed for

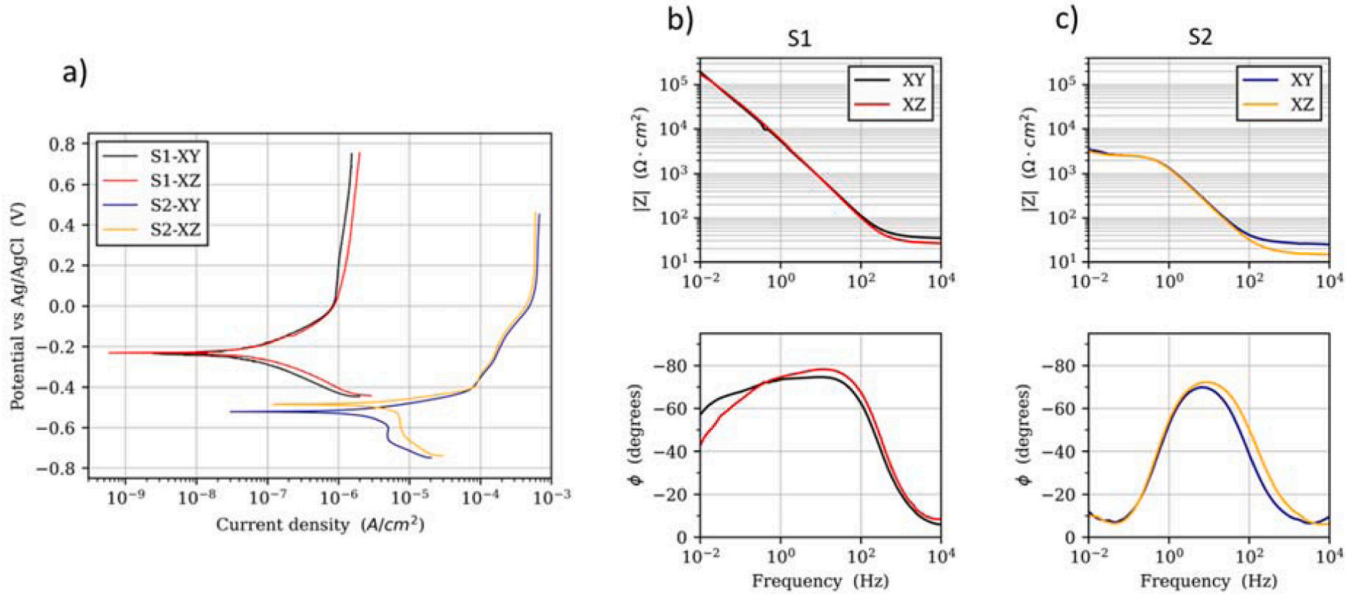

Fig. 6. Electrochemical measurements acquired on heat-treated samples: a) potentiodynamic polarisation curves; b) and c) EIS measurements performed in S1 and S2 solution, respectively. Measurements were acquired on a surface parallel to the printing direction (XZ) and perpendicular to it (XY).

XY and XZ sections. This confirms the hypothesis outlined in the previous section concerning the weak influence of the grain orientation in comparison with the phases present in the material.

3.4. Corrosion mechanism of the alloy

The EIS spectra acquired on the material in the S2 solution, in conjunction with the potentiodynamic polarisation curves and the morphological observations by electron microscopy, allowed the Authors to propose the mechanism for the attack of the Ti6246 alloy.

When in as-built condition, the oxide layer is compact and homogeneous, so the attack occurs uniformly in the alloy microstructure. This behaviour is associated with a finely-dispersed α'' phase inside the β matrix. With this microstructure, the former does not act as a preferential site for the corrosion attack; thus, the oxide layer does not suffer from this heterogeneity. It is worth noticing that many previous studies reported the detrimental effect of the martensitic α' phase on the corrosion behaviour of biphasic titanium alloys produced by additive manufacturing [15,29]. As demonstrated in the present work, this is not the case for the α'' phase in the Ti6246 alloy. The reason may be attributed to the different electrochemical behaviour of α' and α'' phases or to the different phase amounts in the alloys. Further investigations should be performed on this point, but these findings are consistent with the results obtained in a previously published study, where an α'' + β Ti-alloy demonstrated to have a better corrosion resistance with respect to Ti-alloys composed of martensitic α' phase [30].

In the EIS measurements, the spectrum acquired on as-built material is characterised by a single time constant, as can be observed from the Nyquist plot in Fig. 7, exhibiting a single semicircle. This electrochemical system was modelled using the EEC reported in Fig. 8, which is composed of R_s, representing the solution resistance and the parallel of the oxide resistance and capacitance (R_{ox} and CPE_{ox}, respectively). The oxide capacitance was modelled as a Constant Phase Element (CPE) to consider possible non-idealities and time-constant dispersion [31].

Values computed for the 3 parameters are reported in Table 5. As the XZ and XY sections had the same behaviour (see previous section for further details), the reported average and standard deviations are related to the dataset, including both kinds of samples.

The oxide resistance is above 3 kOhm·cm^2, demonstrating its good protective effectiveness in the aggressive solution. Moreover, the computed effective capacitance is 113 μF·cm^{-2}, and thus the estimated oxide thickness is about 0.7 nm.

The morphology of the attack was further investigated using potentiostatic polarisation for 30 minutes in the S2 solution at the potential of −300 mV vs Ag/AgCl, i.e. in the anodic branch of the curve, where an active behaviour is present. FESEM images acquired at the end

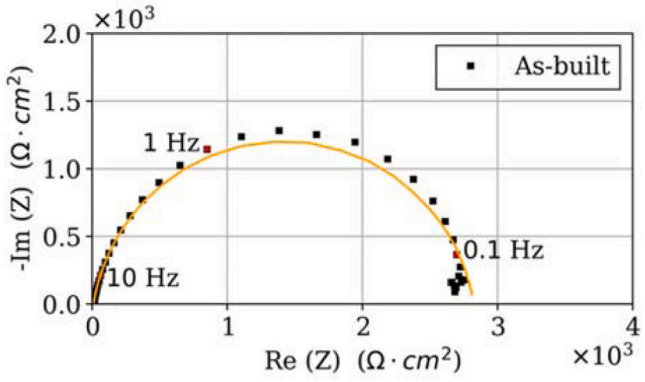

Fig. 7. Impedance spectrum acquired on as-built sample immersed in S2 solution. Black dots represent the experimental data, while the model obtained by EEC fitting (using the electrical circuit reported in Fig. 8) is represented by the yellow line.

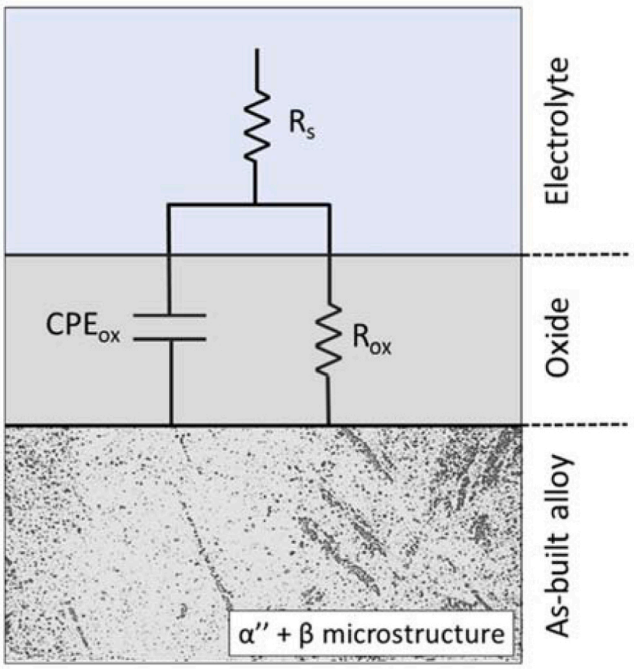

Fig. 8. Equivalent Electrical Circuit model used to fit the impedance spectra acquired on as-built samples immersed in S2 solution. The microstructure of the alloy represents an area of about 6.0 ×2.7 μm^2; the thickness of the oxide layer is not in scale.

Table 5
EEC parameters for as-built samples immersed in S2 solution. See Fig. 8 for the meaning of the circuit parameters.

AB samples	
R_s [Ohm·cm^2]	24.8 ± 16.0
R_{ox} [Ohm·cm^2]	(3.6 ± 0.9) 10^3
Q_{ox} [s^n/Ohm·cm^2]	(1.2 ± 0.1) 10^{-4}
n_{ox}	0.90 ± 0.01

of the test are reported in Fig. 9. As can be seen, the attack proceeds almost uniformly on the alloy, and some of the α'' domains are etched. This is in agreement with the EEC model chosen for the material.

The corrosion mechanism is more complex in the heat-treated material. Actually, in this case, the presence of large α phase domains leads

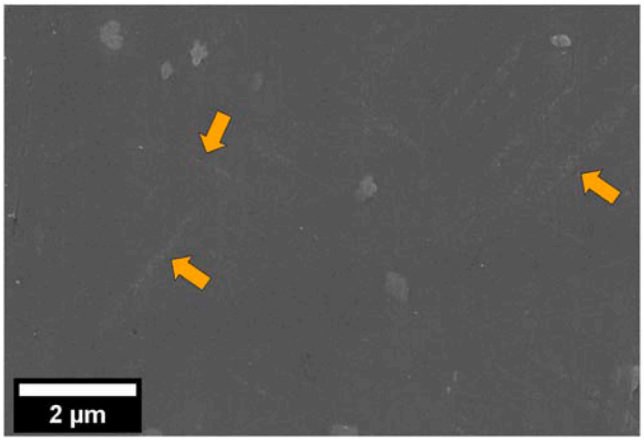

Fig. 9. FESEM micrograph acquired after potentiostatic polarisation at −300 mV on as-built material immersed in S2 solution. Some of the α'' domains are pointed by the 3 arrows.

to a preferential attack in these areas. Thus, the EIS spectrum is characterised by two time constants: the first observed at high frequencies, attributed to the oxide layer, and the second one, attributed to the corrosion reactions occurring on the α phase, observed in the low-frequency part of the spectrum. These two features are visible in the Nyquist plot as two semicircles (see Fig. 10). Thus, the ECC that models this electrochemical system is the one reported in Fig. 11, which is composed of R_s to represent the solution resistance, the parallel of R_{ox} and CPE_{ox} to model the oxide layer, and R_{ct} and CPE_{dl} to model the resistance to charge transfer and capacitance of the double layer associated to the corrosion reactions occurring in correspondence of the α phase domains. Also in this case, all capacitors were modelled as CPE. The values for all parameters (referring to both the XZ and XY sections) are reported in Table 6.

As can be seen, the values for the parameters associated with the oxide layer (namely R_{ox} and Q_{ox}) are similar for the as-built and heat-treated samples. In this case, the effective capacitance is 111 μF·cm^{-2}, and thus, the computed oxide thickness was again about 0.7 nm.

As far as the faradic process is concerned, associated with the preferential attack on the α phase, it is possible to observe that it exhibits a lower resistance (R_{ct}) and a higher capacitance (Q_{dl}).

A potentiostatic polarisation clearly highlighted the morphology of the attack at a potential value in the active region. For this reason, a set of samples was morphologically characterised by electron microscopy after potentiostatic polarisation for 30 minutes in S2 solution at the potential of −300 mV vs Ag/AgCl. The result is reported in Fig. 12. The morphology of the attack is clearly preferential, and it affects mainly the α phase domains, while the β phase network remains almost unaltered. This observation further confirms the origin of the passivation and re-activation phenomena observed in the anodic branch of the potentiodynamic curve (potential range from −390 mV vs Ag/AgCl to +70 mV vs Ag/AgCl). Actually, the presence of the α + β microstructure does not allow a uniform passivation process, but it occurs gradually: the behaviour of the α phase at a potential between – 390 mV and +70 mV is not passive yet.

4. Conclusions

This study characterised the corrosion behaviour of Ti6246 samples produced by PBF-LB/M. It has been demonstrated that, despite the pronounced anisotropic microstructure characterising the as-built condition, the material exhibits the same electrochemical behaviour both in the surface parallel to the printing direction and in the one perpendicular to it. Therefore, grain directionality was proven not to have a marked influence on the corrosion behaviour of the Ti6246 alloy processed by PBF-LB/M. In contrast, a modification of the electrochemical behaviour was found after heat treatment. While the EBSD analysis

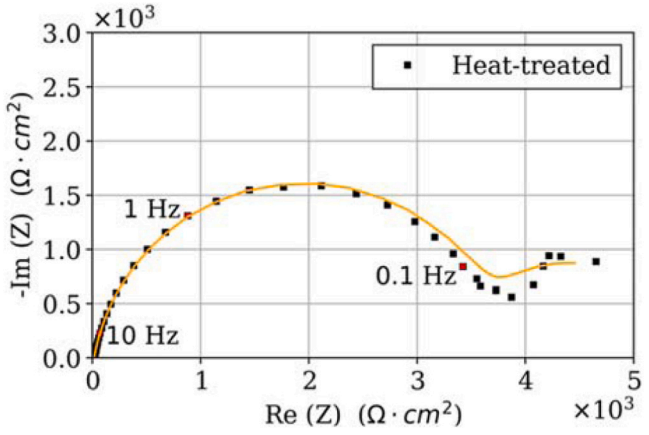

Fig. 10. Representative EIS spectrum acquired on heat-treated samples immersed in S2 solution. The experimental data are represented by black dots, while the model obtained by EEC fitting (using the electrical circuit reported in Fig. 11) is represented by the yellow line.

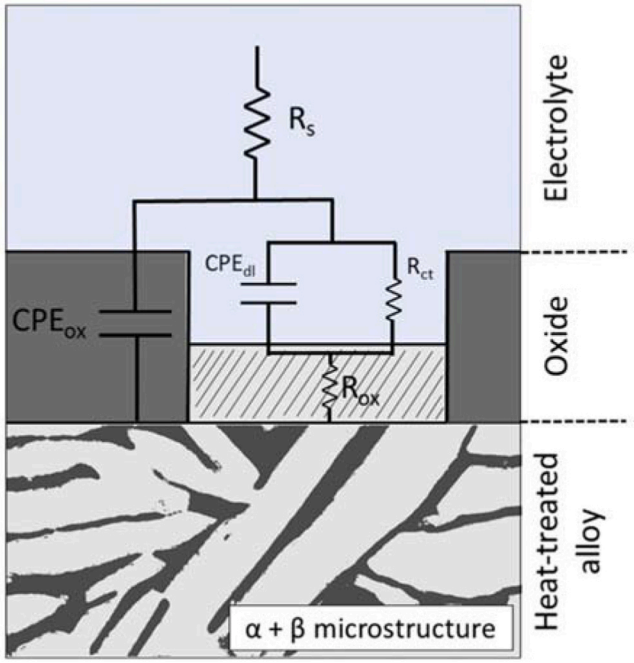

Fig. 11. Equivalent Electrical Circuit model used to fit the impedance spectra acquired on heat-treated samples immersed in S2 solution. The microstructure of the alloy represents an area of about 6.0 ×2.7 μm^2; the thickness of the oxide layer is not in scale.

Table 6
EEC parameters computed for heat-treated samples. See Fig. 11 for the meaning of the circuit parameters.

HT samples	
R_s [Ohm·cm^2]	23.4 ± 9.5
R_{ox} [Ohm·cm^2]	(2.9 ± 0.5) 10^3
Q_{ox} [s^n/Ohm·cm^2]	(1.2 ± 0.5) 10^{-4}
n_{ox}	0.91 ± 0.04
R_{ct} [Ohm·cm^2]	(1.1 ± 0.4) 10^3
Q_{dl} [s^n/Ohm·cm^2]	(1.5 ± 0.5) 10^{-2}
n_{dl}	1.0 ± 0.0

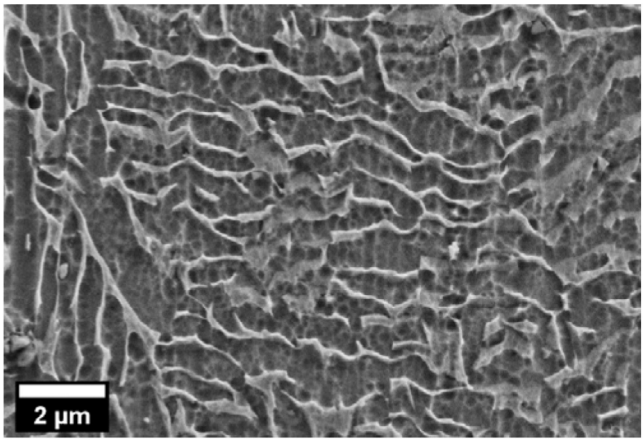

Fig. 12. FESEM characterisation of heat-treated samples after potentiostatic polarisation at −300 mV in S2 solution.

revealed only a less pronounced anisotropic state of the microstructure and an incipient recrystallisation after heat treatment, it showed the almost total transformation from α'' to α + β, confirming the results obtained from the XRD spectrum analysis. This phase transformation was correlated to changes in corrosion mechanisms. Specifically, after heat treatment, the corrosion attack targeted preferentially the α phase, which is less noble than the other phases present. This change in the morphology of the attack was observed only in the electrolyte solution containing both chlorides and fluoride ions, as it is the most aggressive and the only one able to etch the microstructure. Moreover, it is important to underline that the modification in the corrosion mechanism did not significantly impact the corrosion rate, which is estimated by the corrosion current density and the impedance modulus. Thus, the Ti6246 alloy produced via PBF-LB/M demonstrated good corrosion resistance, even when tested in aggressive electrolytes containing fluoride ions.

CRediT authorship contribution statement

Sabrina Grassini: Writing – review & editing, Supervision, Funding acquisition. **Mariangela Lombardi:** Writing – review & editing, Supervision, Funding acquisition. **Leonardo Iannucci:** Writing – review & editing, Writing – original draft, Investigation, Data curation. **Alessandra Martucci:** Writing – review & editing, Writing – original draft, Investigation, Data curation.

Declaration of Competing Interest

The Authors declare that they have no known competing financial interests or personal relationships that could have appeared to influence the work reported in this paper.

Data availability

Data will be made available on request.

Acknowledgments

The Authors gratefully acknowledge the work of Alessia Arcieri, who performed part of the experimental work during her Master's degree thesis.

Appendix A. Supporting information

Supplementary data associated with this article can be found in the online version at doi:10.1016/j.jallcom.2024.176746.

References

[1] T.P. Chapman, V.A. Vorontsov, A. Sankaran, D. Rugg, T.C. Lindley, D. Dye, The Dislocation Mechanism of Stress Corrosion Embrittlement in Ti-6Al-2Sn-4Zr-6Mo, Met. Mater. Trans. A Phys. Met. Mater. Sci. vol. 47 (1) (2016) 282–292, https://doi.org/10.1007/s11661-015-3181-0.

[2] Y. wa Luo, M. yong Wang, J. guo Tu, Y. Jiang, S. qiang Jiao, Reduction of residual stress in porous Ti6Al4V by in situ double scanning during laser additive manufacturing, Int. J. Miner., Metall. Mater. vol. 28 (11) (2021) 1844–1853, https://doi.org/10.1007/s12613-020-2212-z.

[3] M.M. Attallah, S. Zabeen, R.J. Cernik, M. Preuss, Comparative determination of the α/β phase fraction in α+β-titanium alloys using X-ray diffraction and electron microscopy, Mater. Charact. vol. 60 (11) (2009) 1248–1256, https://doi.org/10.1016/j.matchar.2009.05.006.

[4] A. Carrozza, A. Aversa, P. Fino, M. Lombardi, A study on the microstructure and mechanical properties of the Ti-6Al-2Sn-4Zr-6Mo alloy produced via Laser Powder Bed Fusion, J. Alloy. Compd. vol. 870 (2021) 159329, https://doi.org/10.1016/j.jallcom.2021.159329.

[5] T. Choda, H. Oyama, S. Murakami, Technologies for Process Design of Titanium Alloy Forging for Aircraft Parts, Kobelco Technol. Rev. (33) (2015) 44–49.

[6] M.S. Hussain, C. Siemers, J. Rösler, Development of a free-machining (β + β) titanium alloy based on Ti-6Al-2Sn-4Zr-6Mo,", Mater. Manuf. Process. vol. 28 (5) (2013) 545–549, https://doi.org/10.1080/10426914.2012.746781.

[7] H. Hassanin, Y. Zweiri, L. Finet, K. Essa, C. Qiu, M. Attallah, Laser powder bed fusion of Ti-6Al-2Sn-4Zr-6Mo alloy and properties prediction using deep learning approaches, Materials 14 (8) (2021) 2056, https://doi.org/10.3390/ma14082056.

[8] W.H. Kan, H. Peng, S. Lim, Y. Zhu, K. Zhang, A. Huang, The mechanisms behind the tribological behavior of titanium alloys processed by laser powder bed fusion sliding against steel, Tribol. Int vol. 180 (January) (2023) 108279, https://doi.org/10.1016/j.triboint.2023.108279.

[9] Y. Guo, T. Jung, Y.L. Chiu, H. Li, S. Bray, P. Bowen, Microstructure and microhardness of Ti6246 linear friction weld, Mater. Sci. Eng. A vol. 562 (2013) 17–24, https://doi.org/10.1016/j.msea.2012.10.089.

[10] H. Peng, S. Wu, W.H. Kan, S.C.V. Lim, Y. Zhu, A. Huang, Rapid hardening response of ultra-hard Ti-6Al-2Sn-4Zr-6Mo alloy produced by laser powder bed fusion, 2023, Scr. Mater. vol. 226 (August) (2022) 115209, https://doi.org/10.1016/j.scriptamat.2022.115209.

[11] A. Carrozza, A. Aversa, P. Fino, M. Lombardi, Towards customized heat treatments and mechanical properties in the LPBF-processed Ti-6Al-2Sn-4Zr-6Mo alloy, Mater. Des. vol. 215 (2022) 110512, https://doi.org/10.1016/j.matdes.2022.110512.

[12] B. Vincent, V. Optasanu, F. Herbst, S. Chevalier, I. Popa, T. Montesin, L. Lavisse, Comparison Between the Oxidation Behaviors of Ti6242S, Ti6246, TiXT Alloys, and Pure Titanium, Oxid. Met. 96 (3) (2021) 283–294, https://doi.org/10.1007/s11085-021-10051-w.

[13] T.P. Chapman, R.J. Chater, E.A. Saunders, A.M. Walker, T.C. Lindley, D. Dye, Environmentally assisted fatigue crack nucleation in Ti-6Al-2Sn-4Zr-6Mo, Corros. Sci. vol. 96 (2015) 87–101, https://doi.org/10.1016/j.corsci.2015.03.013.

[14] S. Joseph, T.C. Lindley, D. Dye, E.A. Saunders, The mechanisms of hot salt stress corrosion cracking in titanium alloy Ti-6Al-2Sn-4Zr-6Mo, 2018, Corros. Sci. vol. 134 (July) (2017) 169–178, https://doi.org/10.1016/j.corsci.2018.02.025.

[15] N. Dai, L. Zhang, J. Zhang, X. Zhang, Q. Ni, Y. Chen, Distinction in corrosion resistance of selective laser melted Ti-6Al-4V alloy on different planes, " *Eval. Program Plann* vol. 111 (2016) 703–710, https://doi.org/10.1016/j.corsci.2016.06.009.

[16] Struers, "Titanium - Proven materialographic knowledge."

[17] H. Liao, W. Watson, A. Dizon, B. Tribollet, V. Vivier, M.E. Orazem, Physical properties obtained from measurement model analysis of impedance measurements, Electro Acta vol. 354 (2020) 136747, https://doi.org/10.1016/j.electacta.2020.136747.

[18] B. Hirschorn, M.E. Orazem, B. Tribollet, V. Vivier, I. Frateur, M. Musiani, Determination of effective capacitance and film thickness from constant-phase-element parameters, Electro Acta vol. 55 (21) (Aug. 2010) 6218–6227, https://doi.org/10.1016/j.electacta.2009.10.065.

[19] O. Gharbi, M.T.T. Tran, M.E. Orazem, B. Tribollet, M. Turmine, V. Vivier, Impedance Response of a Thin Film on an Electrode: Deciphering the Influence of the Double Layer Capacitance, ChemPhysChem vol. 22 (13) (2021) 1371–1378, https://doi.org/10.1002/cphc.202100177.

[20] A. Barroux, J. Delgado, M.E. Orazem, B. Tribollet, L. Laffont, C. Blanc, Electrochemical impedance spectroscopy study of the passive film for laser-beam-melted 17-4PH stainless steel, Corros. Sci. vol. 191 (May) (2021) 109750, https://doi.org/10.1016/j.corsci.2021.109750.

[21] W. Long, S. Zhang, Y. long Liang, M. gui Ou, Influence of multi-stage heat treatment on the microstructure and mechanical properties of TC21 titanium alloy, Int. J. Miner., Metall. Mater. vol. 28 (2) (2021) 296–304, https://doi.org/10.1007/s12613-020-1996-1.

[22] M. Qi, Q. Wang, Y. Ma, Growth behavior and variant selection of grain boundary α in Ti6246, J. Alloy. Compd. vol. 926 (2022) 166883, https://doi.org/10.1016/j.jallcom.2022.166883.

[23] D. Prando, et al., Corrosion of titanium: Part 1: Aggressive environments and main forms of degradation, J. Appl. Biomater. Funct. Mater. vol. 15 (4) (2017) e291–e302, https://doi.org/10.5301/jabfm.5000387.

[24] B. Lindholm-Sethson, B.I. Ardlin, Effects of pH and fluoride concentration on the corrosion of titanium, J. Biomed. Mater. Res A vol. 86 (1) (2008) 149–159, https://doi.org/10.1002/jbm.a.31415.

[25] M. Nakagawa, S. Matsuya, T. Shiraishi, M. Ohta, Effect of fluoride concentration and pH on corrosion behavior of titanium for dental use, J. Dent. Res vol. 78 (9) (1999) 1568–1572, https://doi.org/10.1177/00220345990780091201.

[26] J.R. Chen, W.T. Tsai, In situ corrosion monitoring of Ti-6Al-4V alloy in H2SO 4/HCl mixed solution using electrochemical AFM, Electro Acta vol. 56 (4) (2011) 1746–1751, https://doi.org/10.1016/j.electacta.2010.10.024.

[27] J. Lu, et al., Effect of microstructure characteristic on mechanical properties and corrosion behavior of new high strength Ti-1300 beta titanium alloy, J. Alloy. Compd. vol. 727 (2017) 1126–1135, https://doi.org/10.1016/j.jallcom.2017.08.239.

[28] J. Liu, S. Duan, X. Yue, N. Qu, Comparison of electrochemical behaviors of Ti-5Al-2Sn-4Zr-4Mo-2Cr-1Fe and Ti-6Al-4V titanium alloys in $NaNO_3$ solution, Int. J. Miner. Metall. Mater. 31 (4) (2024) 750–763, https://doi.org/10.1007/s12613-023-2762-y.

[29] N. Dai, L.C. Zhang, J. Zhang, Q. Chen, M. Wu, Corrosion behavior of selective laser melted Ti-6Al-4 V alloy in NaCl solution, Corros. Sci. vol. 102 (2016) 484–489, https://doi.org/10.1016/j.corsci.2015.10.041.

[30] D. Pede, et al., Microstructure and corrosion resistance of novel β-type titanium alloys manufactured by selective laser melting, J. Mater. Res. Technol. vol. 19 (2022) 4598–4612, https://doi.org/10.1016/j.jmrt.2022.07.021.

[31] M.E. Orazem, B. Tribollet. Electrochemical Impedance Spectroscopy, John Wiley & Sons, 2008, https://doi.org/10.1002/9780470381588.